Revista Mexicana de Astronomía y Astrofísica, **42**, 217–228 (2006)

EMISSION LINE RATIOS FROM VARIABLE VELOCITY JET MODELS

P. Kajdič,[1] P. F. Velázquez,[2] and A. C. Raga[2]

Received 2005 November 5; accepted 2006 May 9

RESUMEN

En este artículo, presentamos una red de simulaciones numéricas axisimétricas de jets con velocidad de eyección variable. En estos modelos, suponemos que los jets son eyectados con una velocidad que varía sinusoidalmente, y con una densidad constante. La red de modelos entonces cubre un intervalo de diferentes amplitudes y períodos de la variabilidad de velocidad de eyección. Como las simulaciones incluyen un tratamiento de ionización fuera de equilibrio del gas, podemos hacer predicciones de la emisión en un conjunto de diferentes líneas espectrales. Así, obtenemos razones de las líneas de emisión para los nudos sucesivos a lo largo de los jets (que coresponden a las "superficies de trabajo internas" formadas como resultado de la variabilidad de la velocidad de eyección), las que se pueden comparar con observaciones de las cadenas de nudos a lo largo de jets HH.

ABSTRACT

In this paper we present a grid of axisymmetric numerical simulations of variable ejection velocity jets. In these models we assume that the jets are ejected with a sinusoidally varying ejection velocity and a time-independent ejection density. The grid of models then spans a range of different velocity variability amplitudes and periods. Because the simulations include a treatment of the non-equilibrium ionization state of the gas, we are able to make predictions of the emission in a set of different emission lines. In this way, we obtain predicted emission line ratios for the successive knots along the jets (which correspond to the "internal working surfaces" formed as a result of the ejection velocity variability), which can be compared directly with observations of the chains of knots along HH jets.

Key Words: **ISM: JETS AND OUTFLOWS — ISM: KINEMATICS AND DYNAMICS**

1. INTRODUCTION

Herbig-Haro (HH) objects form a spectroscopically defined category of objects. They are characterized by an emission line spectrum with the presence of strong low ionization lines (e.g., [O I], [N I], and [S II] lines), strong Balmer series lines (principally Hα and Hβ) and possibly also higher ionization lines (e.g., [O II] and even [O III]). An identification of HH objects using this spectroscopic definition was used in order to identify the objects in Herbig's (1974) catalogue, and the same criterion was used for inclusion in Reipurth's (2004) catalogue (with the exception of a few of the included objects which are only visible in the IR).

In the last two decades, most of the observational effort has been directed to obtaining high angular resolution imaging (e.g., with the *HST*, see Reipurth et al. 2002) and spectroscopic (e.g., with field spectrographs, see Lavalley et al. 1997) observations of HH objects. Theoretical models have also been directed at producing spatially resolved emission line maps (e.g., Raga et al. 2002a) and spectra (e.g., Raga et al. 2004).

Even though the study of observed optical line ratios is still present in the more recent literature, the theoretical aspects of this subject have been largely absent (in contrast to the theoretical interpretation of IR lines, which has remained an active subject, see, e.g., Fernandes 2000). This absence of theoretical work is not accidental. The study of the formation of optical emission lines in stationary, plane-parallel shocks received a considerable amount

[1]Instituto de Astronomía, Universidad Nacional Autónoma de México, México, D. F., México.

[2]Instituto de Ciencias Nucleares, Universidad Nacional Autónoma de México, México, D. F., México.

of attention during the past few decades (Hartigan, Raymond, & Hartmann1987), but interest in calculating new models has dwindled because it is not clear that further theoretical contributions can still be made. Because of this, most of the recent theoretical work has focussed on calculating 2D (axisymmetric) or 3D, time-dependent gasdynamic models, or on calculating 1D, time-dependent models (Massaglia, Mignone, & Bodo 2005).

Until now, numerical simulations of HH jets have included either a simple, parametrized cooling function (and no treatment of the ionization state of the gas, see, e.g., Cerqueira & de Gouveia Dal Pino 2004), or else have included a very limited treatment of the ionization and/or chemical state of the gas. Examples of early efforts to calculate emission lines from numerical jet simulations are the papers of Raga (1988), Blondin, Fryxell, & Konigl (1988;1989), and Smith, Suttner & Zinnecker (1997). The predictions made from these models have been limited to emission line maps and/or emission line profiles from only very few emission lines (mainly the Hα and the H_2 1-0 s(1) lines, see, e.g., Völker et al. 1999).

It has only been very recently that it has become possible to compute numerical simulations of HH jets including a description of the ionization state of many elements. For example, Raga et al. (2004) have computed 3D simulations of a precessing jet, from which they make predictions of several emission lines, and then compare the predicted ratios with the observations.

In the present paper, we continue exploring this new possibility of analyzing the line ratios of HH spectra in terms of multi-dimensional jet models. In particular, we focus on obtaining predictions of emission line ratios from models for the chains of aligned knots observed in some HH jets. Examples of such structures are the knot A to O chain of the HH 34 jet (see, e.g., Reipurth et al. 1986; Bührke, Mundt, & Ray 1988) and the A-V chain of HH 111 (see, e.g., Reipurth, Raga,& Heathcote 1992).

We study models in which the knots along the jet correspond to internal working surfaces resulting from an ejection velocity time-variability. Such a scenario has been used in the past in order to model the Hα emission maps (Raga & Noriega-Crespo 1998) and line profiles (Raga et al. 2002a) of HH 34 and HH 111. In the present paper, we compute a grid of axisymmetric models with different amplitudes and periods for a sinusoidal ejection velocity variability. These models include a computation of the non-equilibrium ionization state of the gas (for a description of the numerical and physical aspects of the simulations, see § 2).

TABLE 1

CHARACTERISTICS OF THE MODELS

Model	Δv	τ	n_j	n_{env}
	km s^{-1}	Years	cm^{-3}	cm^{-3}
M1	100	50	100	10
M2	50	50	100	10
M3	30	50	100	10
M4	10	50	100	10
M5	100	100	100	10
M6	50	100	100	10
M7	30	100	100	10
M8	10	100	100	10
M9	10	50	5×10^3	500
M10	30	50	5×10^3	500

Our primary goal is to obtain predictions of the emission line ratios for a set of eleven emission lines: Hα, [N II]λ6583, [N I]λ5198+200, [O I]λ6300, [O II]λ3026+31, [O III]λ5007, [S II]λ4068+76, [S II] λ6716, [S II]λ6731, [S III]λ9069, and [S III]λ9532, for the succesive knots along the jets. These are a subset of the lines included in the compilation of observed emission line ratios of Raga et al. (1996). We present a few selected emission line maps (§ 3) and the full set of predicted line ratios (§ 4). Finally, a qualitative comparison with observations of HH jets is presented in § 5.

2. THE NUMERICAL SIMULATIONS

We have computed a grid of axisymmetric jet models with the yguazú-a adaptive grid code. This code integrates the gasdynamic equations (together with a system of rate equations for an atomic/ionic network) on a binary, adaptive computational grid. The code is described in detail by Raga, Navarro-González, & Villagrán-Muniz (2000). For the present simulations, we have included an ionization network which includes H I/II, He I/II/III, C II/III/IV, N I/II/III, O I/II/III/IV, and S II/III. The H, He, C, and O atoms/ions are considered in the calculation of the radiative cooling term (which is included in the energy equation). A detailed description of the ionization/recombination rates as well as of the cooling rates is given by Raga et al. (2002b). In all of the models, we have assumed relative abundances of H, He, C, N, O = 0.9, 0.1, 3.31×10^{-4}, 9.8×10^{-5}, 6.61×10^{-3}.

The ejection velocity of the material in our models varies sinusoidally with time:

$$v(t) = v_0 + \Delta v \sin\left(\frac{2\pi}{\tau}t\right), \qquad (1)$$

where v_0 = 250 km s^{-1} is the average velocity and is the same in all our models, Δv is the amplitude and τ the period. The amplitude Δv is varied from 100 km s^{-1} (models M1 and M5) down to 10 km s^{-1} (models M4 and M8). We have also explored models with ejection velocity variability periods $\tau = 50$ (models M1-M4) and 100 yr (models M5-M8). The parameters for models M1-M10 are given in Table 1.

All of our jet models have an initially top-hat cross section, with a constant $n_j = 100$ cm^{-3} (models M1-M8) or $n_j = 5 \times 10^3$ cm^{-3} density (models M9 and M10), a $T_j = 1000$ K temperature and $r_j = 10^{15}$ cm radius. The calculations are started applying the initial conditions within a cylinder extending $L = 10^{15}$ cm out from the injection point. The jets are assumed to travel into a homogeneous environment of density $n_{env} = 10$ cm^{-3} and temperature $T_{env} = 1000$ K. Both the initial jet and undisturbed environment are assumed to be neutral, except for C and S which are singly ionized.

We carry out the numerical simulation on a 5-level binary adaptive grid with a maximum resolution of 7.3×10^{13} cm (in both the axial and radial directions). The computational domain has a $(30.0, 3.75) \times 10^{16}$ cm (axial, radial) spatial extent, and transmission conditions are applied on the outer axial and radial boundaries. Reflection conditions are applied on the symmetry axis and on the $z = 0$ plane, outside of the circular jet injection region.

The 7.3×10^{13} cm spatial resolution has to be compared with the cooling distances behind the shocks produced in the internal working surfaces of the jet flows. The internal working surface shocks have shock velocities v_s of the order of the amplitude Δv of the ejection velocity variability (see Eq. 1). From our numerical simulations, we find that the pre-shock densities are typically a factor of 1/10 to 1/2 of the initial jet density (so that $n_{pre} \sim 20$ cm^{-3} for models M1-M8, see above). From the paper of Hartigan et al. (1987), we see that for such a pre-shock density, the cooling distances d_{c4} (to 10^4 K) and d_{c3} (to 1000 K) behind plane-parallel shocks have minimum values $d_{c3} = 7.5 \times 10^{13}$ cm and $d_{c4} = 3.8 \times 10^{14}$ cm for $v_s = 80$ km s^{-1} and go up sharply for increasing or decreasing shock velocities (for example, $d_{c3} = 4.4 \times 10^{15}$ cm and $d_{c4} = 4.8 \times 10^{14}$ cm for $v_s = 40$ km s^{-1}). Basically, the cooling regions behind shocks with v_s close to 80 km s^{-1} are marginally resolved in our simulations, but the regions behind shocks with either larger or lower velocities are appropriately resolved. The high density models (M9 and M10) have internal shocks with shock velocities $\sim 10 \to 30$ km s^{-1}, and cooling distances $\sim 2 \times 10^{14}$ cm, again reasonably resolved in our simulations.

3. MODEL RESULTS

From the numerical simulations described in § 2, we obtain the stratification of the flow variables (pressure, density, temperature, flow velocity, and ionization state of the gas) as a function of position and time. We only analyze the results obtained for $t = 2000$ yr, which corresponds to ≈ 1600 yr after the leading head of the jet has left the computational domain.

From the $t = 2000$ yr flow stratifications, we compute the emission coefficients for eleven emision lines: Hα, [N II]λ6583, [O I]λ6300, [O II]λ3026+31, [O III]λ5007, [S II]λ4068+76, [S II]λ6716, [S II]λ6731, [S III]λ9069, and [S III]λ9532. The Hα emission is calculated adding the contributions of the recombination cascade and the collisional excitations from the ground state (using the $n = 1 \to 3$ collision strength of Giovanardi, Natta, & Palla 1987). The rest of the lines are computed solving 5-level atom problems using the parameters of Mendoza (1983).

These emission coefficients are then integrated along lines of sight (assuming that the jet axis lies on the plane of the sky) to obtain emission maps for all of the lines. In order to illustrate the results that we obtain from our simulations, in Figures 1 and 2 we show the electron density, mass density, temperature and axial velocity stratifications, as well as the maps for all of the predicted emission lines, for model M1.

From these figures, we see that the knots have a high density region of gas trapped between the internal working surface shocks, and that part of this material exits laterally, forming a bow shock against the gas within the cocoon of the jet. The emission line maps have a clear contribution from the extended wings of the bow shock driven by the head of the jet (brigthened, cylindrical emission structure occupying almost all the area of the maps). Superimposed on this emission, we see the emitting knots, which correspond to the successive internal working surfaces of the jet.

Within the computed maps, the $\tau = 50$ yr models (models M1-M4) have six knots (see Fig. 1), and the $\tau = 100$ yr models (models M5-M8, see Table 1)

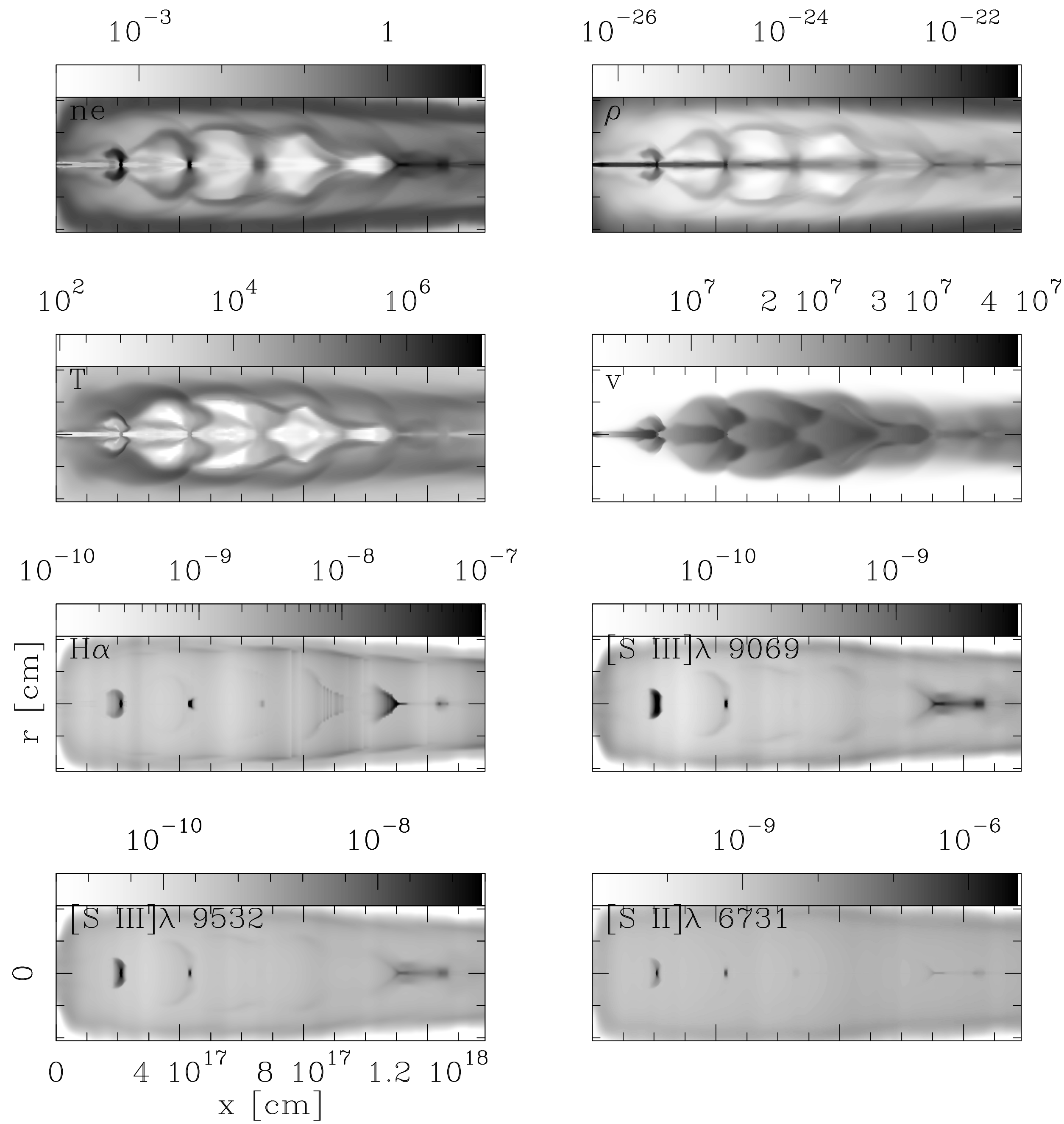

Fig. 1. Results obtained from model M1. On the plots we have: electron density (in cm^{-3}), total density (g cm^{-3}), temperature (K), velocity along the jet (cm s^{-1}) and emission maps for the following emission lines: Hα, [S III]λ9069, [S III]λ9532, and [S II]λ6731 (in units of erg s^{-1}cm^{-2}sterad^{-1}). The small ticks on the axis perpendicular to the jet flow correspond to distances of 10^{17}cm.

have three knots. Some of the knots are not clearly seen against the background (produced by the leading bow shock wings, see above), at least in some emission lines.

For the higher velocity variability amplitude models, the knots are seen in emission lines with a range of ionization levels (e.g., model M1, Fig. 1). The higher ionization lines are absent in the lower

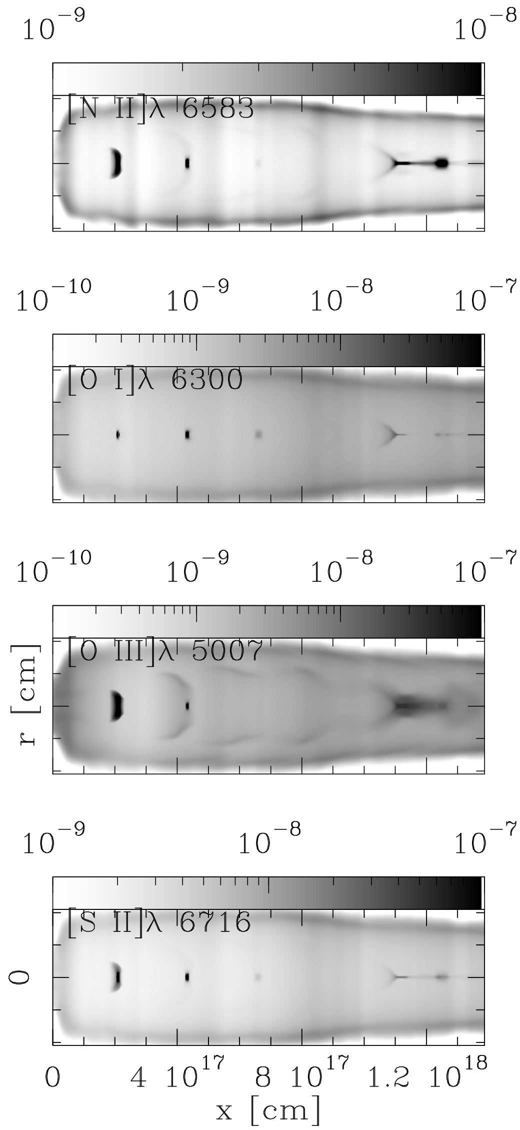

Fig. 2. Emission maps for the following emission lines: [N II]λ6583, [N I]λ5198+200, [O I]λ6300, [O II]λ3726, [O III]λ5007, [S II]λ4068+76, and [S II]λ6716, obtained for model M1 (after a $t = 2000$ yr integration, see § 3) in erg $s^{-1}cm^{-2}sterad^{-1}$.

velocity amplitude models, except in the high density models (M9 and M10), in which the emission from the bow shock wings (of the internal working surfaces) becomes more important.

In Figure 3 we show maps of the spatially resolved emission line ratios [O I]λ6300/Hα, [O II]λ3026+31/Hα, and [O III]λ5007/Hα obtained from model M1. In this figure, we see that the first three knots have an [O I]/Hα line ratio peak in the central region of the internal working surfaces (i.e., in the two working surface shocks within the jet beam), while the bow shock wings (driven into the jet cocoon) correspond to regions of low line ratio values. The [O II]/Hα line ratio shows a peak only in the first two knots, and has a minimum in the in the third and fourth knots.

The [O III]/Hα line ratio has a peak within the jet beam in the first knot, indicating that the shock velocity of one of the two shocks (actually, of the leading shock which has a higher shock velocity, see Raga & Cantó 1998) has a shock velocity exceeding 100 km s^{-1}, which is consistent with the velocity variability amplitude of model M1 (see Table 1). In the knots further away from the source, the shocks within the jet beam have decayed to lower shock velocities, and no longer produce [O III] emission. In-

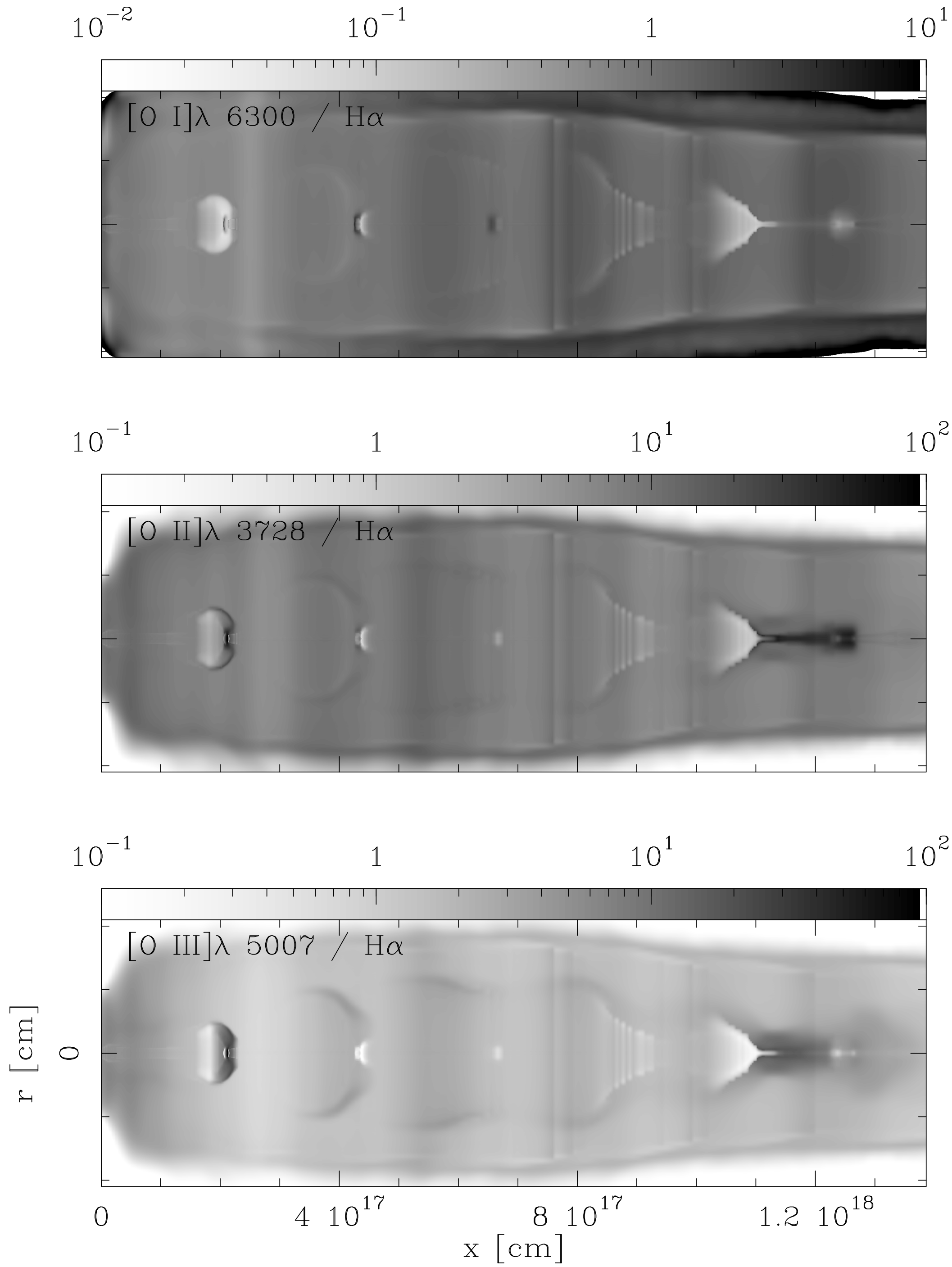

Fig. 3. Emission line ratio maps [O I]λ6300/Hα, [O II]λ3728/Hα, and [O III]λ5007/Hα for model M1.

terestingly, the bow shock wings of these knots do show some level of [O III] emission, even though they are only partially radiative.

As the presence of [O III] emission in knots with low shock velocity internal beam shocks is somewhat surprising, we discuss this result in more detail. In our models, we choose a mean jet velocity $v_0 = 250$ km s^{-1} for all of our models and a velocity variability amplitude $\Delta v = (10 \rightarrow 100)$ km s^{-1} (see Table 1). For an amplitude of $\Delta v = 20$ km s^{-1}, the shocks

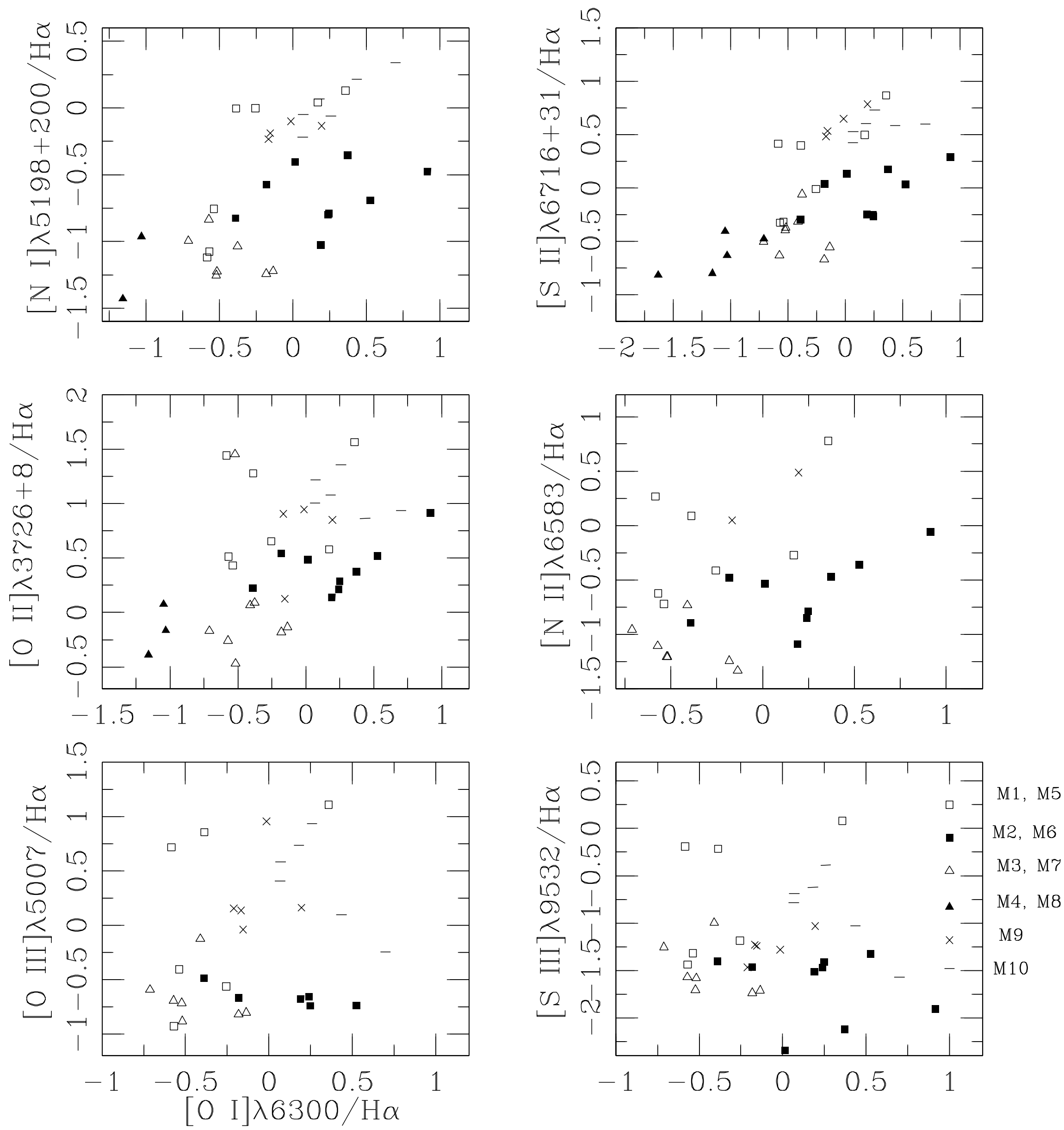

Fig. 4. Logarithmic plots of the emission line ratios calculated with the line intensities of the successive knots (along all of the computed models) as a function of the corresponding [O I]λ6300/Hα line ratio.

within the jet beam associated with the successive working surfaces have a value of at the very most 40 km s^{-1} (and generally have shock velocities substantially smaller than this value). For the beam shocks to emit [O III], one would need to have a variability amplitude at the very least of $\Delta v \approx 50$ km s^{-1}.

However, the working surfaces eject material sideways, and this material produces a bow shock against the cocoon surrounding the jet beam. As one moves away from the beam of the jet, this cocoon has velocities along the jet axis which are substantially lower than the velocity of the jet, and reaches lower velocity values when one goes out towards the long wings of the leading bow shock (this effect is discussed in a quantitative way by Raga et al. 2002c). Therefore, the shock velocities associated with the wings of the internal working surface bow shocks can be quite high (i.e., a substantial fraction of the mean velocity of the jet, with values above 100 km s^{-1}) and [O III] emission can be produced.

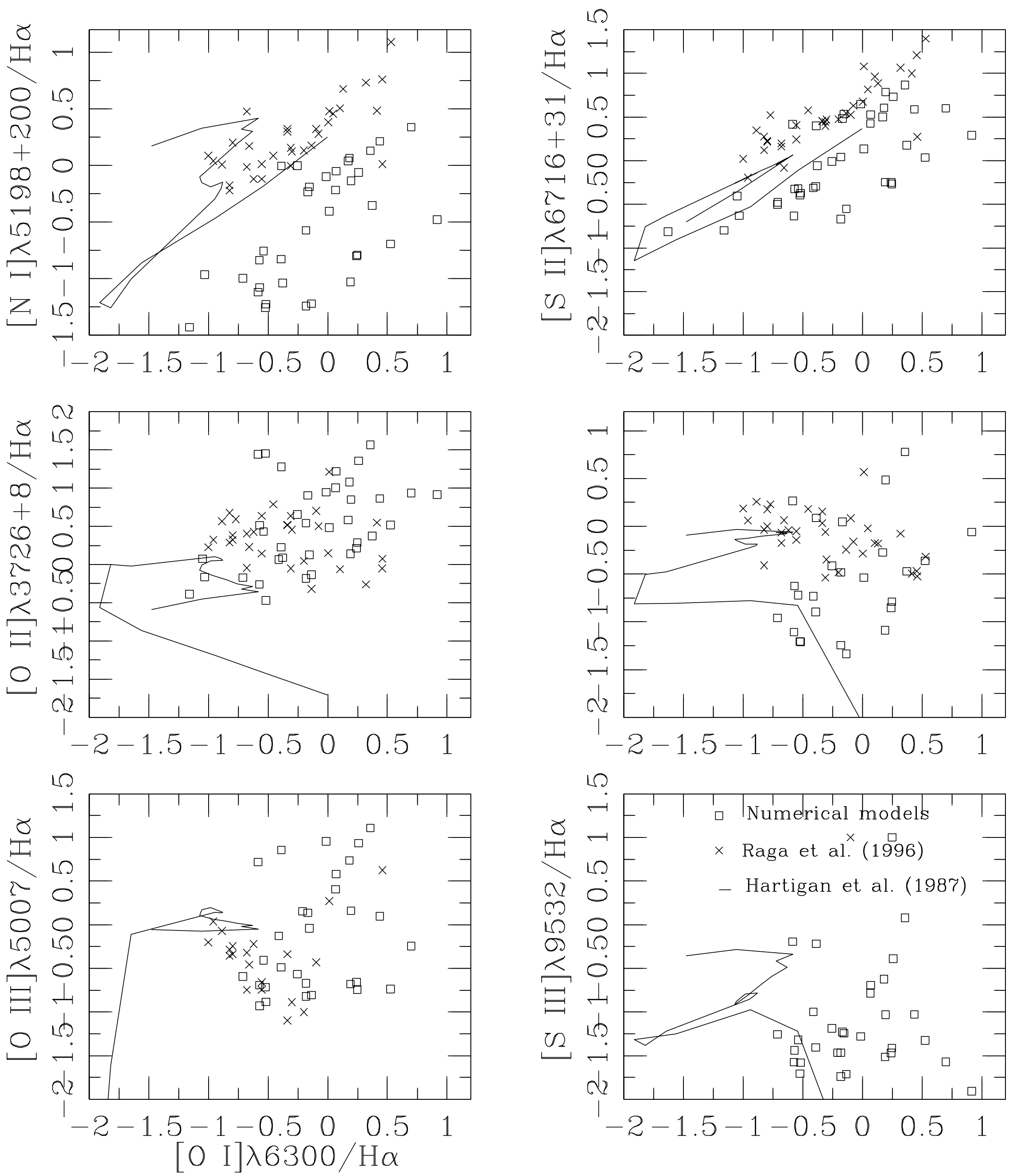

Fig. 5. Comparison of our results (open squares) with the observational data from Raga, Böhm, & Cantó (1996) (crosses) and the plane-parallel shock models from Hartigan et al. (1987) (solid lines). In general, our predictions agree well with the observational data, except for the high-velocity models (M4 and M8) and high-density models (M9 and M10). The plots are logarithmic.

Interestingly, the emission from these high velocity bow shock wings is strongly dependent on the density of the environment. For the lower density environment models (models M1-M8, see Table 1), the cocoon has a typical density of 0.1 cm^{-3}. For this pre-shock density and a shock velocity of 100–160 km s^{-1}, the models of Hartigan et al. (1987) give a cooling distance $d_4 = (1 \to 4) \times 10^{16}$ cm. Therefore, these bow shock wings are only partially radiative (since the internal working surface bow shocks have a radius of $\sim 10^{17}$ cm, which is comparable to the cooling distance d_4). Because of this, the contribution to the total emission from the bow shock wings becomes much more important for the denser models (models M9-M10), in which the cocoon is denser, and therefore the bow shocks are more radiative.

4. LINE INTENSITIES AND LINE RATIOS

In order to obtain the luminosity of the successive knots for a given emission line, we place on the knot a circular diaphragm of an appropriate radius r_d and obtain the integrated line intensity I_d within the diaphragm. We then repeat this process for a circular diaphragm of radius $r_b = 1.3 r_d$ to obtain an integrated intensity I_b. With these two integrated intensities we then obtain the emission contributed by the knot:

$$I_{knot} = \frac{{r_b}^2 I_d - {r_d}^2 I_b}{{r_b}^2 - {r_d}^2} \,. \qquad (2)$$

In Table 2, we present the luminosities of the different emission lines in the successive knots as ratios to the corresponding Hα luminosities (also listed in the table) for all of the computed models. In order to show the general behaviour of the line ratios, we have plotted them in different ways.

First, in Figures 4 and 5 we show the logarithmic plots [N I]λ5198+200/Hα, [O II]λ3728+29/Hα, [O III]λ5007/Hα, [N II]λ6583/Hα, [S II]λ6716+31/Hα, and [S III]λ9532/Hα ratios as a function of the [O I]λ6300/Hα line ratio (the graph showing all of the values listed in Table 2). In this graph, we see that the low ionization lines ([N I]λ5198+200 and [S II]λ6716+31) show trends of increasing line ratios (with respect to Hα) as a function of increasing [O I]λ6300/Hα.

The high ionization lines ([O III]λ5007 and [S III]λ9532) have line ratios with a large scatter. Interestingly, the knots with [O III]λ5007/H$\alpha > 0.5$ and [S III]λ9532/H$\alpha > 0.2$ correspond either to the large amplitude velocity variability models (models M1 and M5, with $\Delta v = 100$ km s^{-1}) or to the "dense" models (M9 and M10, with $n_j = 5000$ cm^{-3}). All of the other models have knots with either zero or very low [O III]λ5007/Hα and [S III]λ9532/Hα line ratios.

The intermediate ionization lines ([O II]λ3726 +29 and [N II]λ6583) show a clear trend of increasing ratios to Hα for [O I]λ6300/H$\alpha < 0.3$ (see Fig. 1). For larger values of [O I]λ6300/Hα, the intermediate ionization lines have line ratios with a wide scatter of values.

In Fig. 5, we present a comparison between the line ratios predicted for the knots of our jet models (see also Table 2), the "self-consistent preionization", stationary, plane-parallel shock models of Hartigan et al. (1987) and the line ratios of HH objects compiled by Raga et al. (1996). From this figure, we see that in general our model predictions show a wider scatter than the line ratios from the plane-parallel shock models. This is in principle not surprising since the emission from the knots along the jets in our numerical simulations comes from a superposition of shocks with complex geometries and time-dependent characteristics. The fact that this complexity results in a wider range of line ratios than the ones predicted from stationary, plane-parallel shock models might have been expected.

At the same time, however, some of the trends in the line ratios appear to be shared by our jet models and by the plane-parallel shock models. This is particularly true for the [N I]λ5198+200/Hα and [S II]λ6716+31/Hα versus [O I]λ6300/Hα plots (see Fig. 4).

In these plots ([N I]λ5198+200/Hα and [S II]λ6716+31/Hα versus [O I]λ6300/Hα), we also find a good agreement between the observed line ratios and the predictions from our models, with both the trends and the scatter in the line ratios being very similar. However, the observations show the existence of a few objects with $10^{0.90} <$[S II]λ6716+31/Hα $<10^{1.11}$, while the largest predicted value corresponds to a line ratio of $\approx 10^{0.90}$ (see Fig. 5 and Table 2).

The observed and predicted [N II]λ6583/Hα and [O II]λ3726+29/Hα ratios do not show clear trends as a function of [O I]λ6300/Hα. The [N II]λ6583/Hα versus [O I]λ6300/Hα plot (see Fig. 2) has a similar scatter of points in both the observations and in our model predictions. However, the predicted [O II]]λ3726+29/Hα ratios show a number of points with values above $10^{0.78}$, while no such values have been observed. As can be seen from Fig. 5, these values mostly correspond to the "dense" models (M9 and M10), which would therefore not be appropriate for modelling the observed objects.

The [O III]λ5007/Hα and [S III]λ9532/Hα ratios predicted for some of the knots of our models have values above 10^0 or above $10^{-0.7}$ (for the [O III]λ5007/Hα and the [S III]λ9532/Hα ratios, respectively) which are never observed (see Fig. 5). These high predicted [O III]λ5007/Hα and [S III]λ9532/Hα ratios correspond either to our larger amplitude velocity variability (M1 and M5) or

TABLE 2

RESULTS OF THE NUMERICAL MODELS

		Hα 6563	[N I] 5198 +200	[N II] 6583	[O I] 6300	[O II] 3726 +8	[O III] 5007	[S II] 4068 +76	[S II] 6716	[S II] 6731	[S III] 9069	[S III] 9532
	x (cm)	$L/L_\odot$	$L/L_{\mathrm{H}\alpha}\cdot 100$									
M1												
	4.41e+16	2.37e-08	99.1	123	41	1900	718	29.3	144	107	24.5	60.7
	9.38e+16	1.01e-08	99.6	38.5	55.6	452	27.3	10.3	57.4	40.6	2.63	6.53
	1.44e+17	1.13e-10	110	53.3	148	382	···	20.1	200	116	···	···
	2.32e+17	1e-08	80.5	···	···	271	···	1.64	10	5.63	3.08	6.43
	2.67e+17	3.18e-10	135	601	228	3680	1280	62.9	422	315	67.7	120
M2												
	4.25e+16	1.86e-07	33.3	87.4	825	825	0.07	23.7	108	87.7	0.5	1.24
	8.71e+16	1.24e-08	44.4	33.8	236	237	0.28	12.5	87.3	62.7	0.34	0.76
	1.31e+17	2.29e-09	20.3	43.6	336	329	18.3	8.47	62.6	46	2.33	4.76
	1.76e+17	2.9e-09	9.39	8.16	155	138	20.9	3.24	37.6	19.1	1.19	3.08
	2.22e+17	3.65e-09	15.9	14.1	174	163	22	4.29	31	25.3	1.64	3.4
	2.71e+17	7.26e-09	16.2	16.3	177	194	18.1	5.59	36.1	18.1	1.4	3.88
M3												
	8.37e+16	3.62e-10	9.2	···	42.0	122.9	···	59.9	51.6	35.9	···	···
	1.24e+17	1.54e-09	6.0	6.2	30.3	33.8	13.1	24.0	25.714	16.688	1	2.6
	1.67e+17	3.46e-09	5.6	6.2	30.1	45.4	19.22	20.3	23.6	16.6	1.1	2.0
	2.11e+17	3e-09	14.6	7.8	26.8	55	20.3	17.5	14.1	9.267	1.4	2.7
	2.51e+17	3.25e-09	10.1	11.0	19.4	67.7	25.5	16.0	19.0	12.6	1.5	5.6
	2.9e+17	2.57e-09	···	18.5	38.9	116.7	74.7	32.5	28.6	20.2	3.3	10.0
M4												
	7.93e+16	5.21e-10	···	···	···	···	···	···	···	···	···	···
	1.21e+17	6.56e-10	···	···	3.2	···	···	0.713	···	···	···	···
	1.61e+17	1.06e-09	···	···	2.3	···	···	0.9	10	5.4	···	···
	2.02e+17	6.47e-10	···	···	8.9	118.9	···	2.5	25.5	13.9	···	···
	2.41e+17	1.62e-09	10.9	···	9.3	68.5	···	1.5	12.8	10.6	···	···
	2.81e+17	3.08e-09	3.7	···	6.9	40.9		1.0	10.5	5.5	···	···
M5												
	8.64e+16	4.98e-08	7.6	184.5	26.04	2777.1	521.9	34.1	147.0	114.1	25.9	64.3
	1.67e+17	1.47e-08	8.4	23.7	27.0	327.0	11.8	5.6	26.9	20.5	1.5	3.7
	2.51e+17	5.76e-09	17.6	19.0	29.0	270.2	39.4	5.3	28.3	20	3.0	4.8
M6												
	8.21e+16	2.05e-07	39.6	29.1	103.2	305.3	0.1	14.8	78.3	58.5	0.2	0.5
	1.67e+17	2.42e-08	26.7	33.1	65.9	349.5	21.4	10.8	64.4	45.5	1.5	3.4
	2.57e+17	1.16e-08	14.9	12.7	40.7	168.1	32.6	4.8	29.4	21.5	1.5	3.9
M7												
	1.63e+17	4.42e-09	6.0	4.6	73.3	73.3	15.7	2.5	16.8	11.2	0.7	1.9
	2.47e+17	1.12e-08	5.7	5.7	65.9	65.9	15.2	2.0	13.6	7.9	0.8	1.8
M8												
	1.62e+17	2.67e-10	···	···	···	···	···	···	···	···	···	···
	2.37e+17	7e-10	···	···	19.6	···	···	2.5	18.1	15.3	···	···
M9												
	8.13e+16	4.89e-08	···	···	···	···	···	···	···	···	···	···
	1.23e+17	9.93e-08	···	···	61.7	···	143.0	···	···	···	1.1	3.4
	1.63e+17	1.43e-07	64.6		70.1	133.6	91.4	20.3	169.5	172.8	2.6	5.7
	2.03e+17	2.65-07	58.5	111.6	68.1	806.5	136.7	18.6	153.2	151.1	2.9	5.9
	2.45e+17	4.39e-07	73.5	306.5	156.8	711.2	145.2	28.2	334.1	276.1	2.1	9.3
	2.85e+17	6.48e-07	79.6		96.9	886.1	90.2	28.8	128.3	317.6	1.5	5.3
M10												
	8.43e+16	9.87e-07	218.7	···	501.3	865.9	56.8	81.2	397.6	···	1.0	2.7
	1.27e+17	1.54e-06	163.9	···	272.9	733.5	125.5	45.8	386.8	···	3.8	9.4
	1.7e+17	1.71e-06	60.7	···	116.6	1010.2	255.4	32.6	266.2	···	6.3	16.4
	2.11e+17	1.81e-06	89.2	···	117.6	1665.5	381.0	39.1	337.1	···	7.9	20.4
	2.51e+17	1.2e-06	116.6	···	151.8	1207.0	544.4	40.9	403.8	···	13.3	23.9
	2.96e+17	4.68e-07	87.1	···	181.4	2283.2	858.2	43.1	538.9	···	17.5	40.9

to our denser (M9 and M10) models (see above and Fig. 5).

Table 2 shows the results of our models. The line intensities are shown as ratios Hα multiplied by a factor of 100. The columns of the table show: 1) the name of the model, 2) the x-coordinate of the knots (defined as the positions along the jet axis of the corresponding Hα peaks), 3) the luminosities of the Hα line, and 4) the ratio between the luminosity of each line and Hα. If the number does not appear it means that the knot was not visible in the given emission line. This is common for high ionization lines (e.g., [O III], [O II], [N II], and [S III] lines) in the low velocity amplitude models M4 and M8.

5. CONCLUSIONS

We have computed a grid of ten axisymmetric numerical simulations of sinusoidally variable ejection velocity jets. In the simulations we varied the amplitude and period of the ejection velocity and the density of the jets. We used the yguazú-a adaptive grid code, which integrates the gasdynamic equations together with a set of rate equations for a number of different atoms and ions (see § 2) in a binary, adaptive computational grid. From these models, we obtained predictions of emission line maps for a set of eleven emission lines with different excitations, which show the successive emission line knots along the jets.

From the emission maps predicted from our model jets, we have obtained the emission line luminosities for the successive knots along the jets (see Table 2). We then present these intensities as ratios of the computed lines to Hα as a function of the [O I]λ6300/Hα ratio (see Figs. 4 and 5). These two-line ratio plots are compared with the predictions from the plane-parallel shock wave models of Hartigan et al. (1987) and with the compilation of observational results of Raga et al. (1996).

We find that the line ratios predicted from our jet models cover regions in the two-line ratio plots larger than the predictions from the plane-parallel models (see Fig. 5). This is not surprising given the wide range of time-dependent shock geometries which are present in the knots in our jet simulations. In Fig. 3 we show as examples of the line ratio maps for three emission lines: [O I]λ6300, [O II]λ3026+31, and [O III]λ5007.

For the ratios of the low ionization lines ([N I] and [S II]) to Hα as a function of [O I]λ6300/Hα we find a good agreement in the trend and scatter of the predictions and of the observations. For the high ionization lines the agreement is not so good, because our jet models with higher densities and velocity variability amplitudes produce [O III]/Hα and [S III]/Hα ratios which are significantly higher than the observed values.

We should note that some of our low Δv models (notably, models M9 and M10 with $\Delta v = 10$ and 30 km s^{-1}) produce strong [O III] 5007 emission. This emission of course does not come from the internal working surface shocks within the jet beam (which have typical shock velocities of $\sim$ 30 km s^{-1} and therefore produce no [O III] emission), but is produced in the bow shocks driven by the working surface into the jet cocoon. These bow shocks can have substantial shock velocities (up to a substantial fraction of the value of the mean jet velocity of 250 km s^{-1}), and become more radiative for increasing environmental densities, therefore contributing more to the emission from the successive knots.

The work described in this paper is a first effort at modelling the line ratios of HH objects in terms of a full, axisymmetric gasdynamic model. The line ratios which we have calculated can be compared with the ones observed in individual HH objects, in order to determine which are the model parameters which best fit the observed object. Comparisons of this type will be useful, because it will then be possible to evaluate whether or not the deduced jet parameters (needed to reproduce the observed line ratios) are consistent with the dynamical properties (deduced from the observed radial velocities and proper motions) of the objects.

An evident problem in the models which we are presenting is that variable ejection jets have a large number of free parameters. Our models are restricted to a limited range of jet (ejection velocity periods and amplitudes, mean jet velocities, densities and temperatures) and environmental (density and temperature) parameters. Also, they are limited to the case of a jet with a sinusoidally varying ejection velocity, moving into a uniform environment. Furthermore, our jets are not magnetized.

In future work we will study a wider range of jet models. These will include extending the parameter space, including a dynamically important magnetic field, studying other forms of the ejection variability (including different functional forms for the velocity variability, as well as also considering a variable density), and considering a stratified environment. We should note that the effects on the line emission of different forms of the ejection variability (Hartigan & Raymond 1993) and of the presence of magnetic fields (Massaglia et al. 2005) have already been explored in terms of 1D, variable jet models.

This work was supported by the CONACyT grants 41320-F and 43103-F and the DGAPA (UNAM) grant IN 113605. Primož Kajdič acknowledges the Dirección General de Estudios de Posgrado of the UNAM for a scholarship supporting his graduate studies.

REFERENCES

Blondin, J. M., Konigl, A., & Fryxell, B. A. 1988, BAAS, 20, 909
__________. 1989, ApJ, 337, 37
Bührke, T., Mundt, R., & Ray, T. P. 1988, A&A, 200, 99
Cerqueira, A. H., & de Gouveia Dal Pino, E. M. 2004, A&A, 426, 25
Fernandes, A. J. L., 2000, MNRAS, 315, 657
Giovanardi, C., Natta, A., & Palla, F. 1987, A&A, 70, 269
Hartigan, P., & Raymond, J. 1993, ApJ, 409, 705
Hartigan, P., Raymond, J., & Hartmann, L. 1987, ApJ, 316, 323
Lavalley, C., Cabrit, S., Dougados, C., Ferruit, P., & Bacon, R. 1997, A&A, 327, 671
Massaglia, S., Mignone, A., & Bodo, G. 2005, A&A, 442, 549
Mendoza, C. 1983, in IAU Symp. 103, Planetary Nebulae, ed. D. R. Flower (Dordrecht: Reidel), 143
Raga, A. C. 1988, ApJ, 335, 820
Raga, A. C., Böhm, K.-H., & Cantó, J. 1996, RevMexAA, 32, 161
Raga, A. C., & Cantó, J. 1998, RevMexAA, 34, 73
Raga, A. C., de Gouveia dal Pino, E. M., Noriega-Crespo, A., Mininni, P., & Velázquez, P. F. 2002b, A&A, 392, 267
Raga, A. C., Navarro-González, R., & Villagrán-Muniz, M. 2000, RevMexAA, 36, 67
Raga, A. C., & Noriega-Crespo, A. 1998, AJ, 116, 2943
Raga, A. C., Riera, A., Masciadri, E., Beck, T., Böhm, K. H., & Binette, L. 2004, AJ, 127, 1081
Raga, A. C., Velázquez, P. F., Cantó, J., & Masciadri, E. 2002a, A&A, 395, 647
__________. 2002c, RevMexAA, 38, 251
Reipurth, B., Bally, J., Graham, J. A., Lane, A. P., & Zealy, W. J. 1986, A&A, 164, 51
Reipurth, B., Raga, A. C., & Heathcote, S. 1992, ApJ, 392, 145
Reipurth, B., Heathcote, S., Morse, J., Hartigan, P., & Bally, J. 2002, AJ, 123, 362
Smith, M. D., Suttner, G., & Yorke, H. W. 1997, A&A, 323, 223
Völker, R., Smith, M. D., Suttner, G., & Yorke, H. W. 1999, A&A, 343, 953

Primož Kajdič: Instituto de Astronomía, UNAM, Apdo. Postal 70-264, 04510 México, D. F., México (primoz@astroscu.unam.mx).
Alejandro C. Raga and Pablo F. Velázquez: Instituto de Ciencias Nucleares, UNAM, Apdo. Postal 70-543, 04510 México, D. F., México (raga, pablo@nucleares.unam.mx).